

Ultra-High-Definition Image Restoration: New Benchmarks and A Dual Interaction Prior-Driven Solution

Liyan Wang¹ · Cong Wang² · Jinshan Pan³ · Xiaofeng Liu⁴ ·
Weixiang Zhou¹ · Xiaoran Sun¹ · Wei Wang⁵ · Zhixun Su^{1,6}

Received: date / Accepted: date

Abstract Ultra-High-Definition (UHD) image restoration has acquired remarkable attention due to its practical demand. In this paper, we construct UHD snow and rain benchmarks, named UHD-Snow and UHD-Rain, to remedy the deficiency in this field. The UHD-Snow/UHD-Rain is established by simulating the physics process of rain/snow into consideration and each benchmark contains 3200 degraded/clear image pairs of 4K resolution. Furthermore, we propose an effective UHD image restoration solution by considering gradient and normal priors in model design thanks to these priors' spatial and detail contributions. Specifically, our method contains two branches: (a) feature fusion and reconstruction branch in high-resolution space

and (b) prior feature interaction branch in low-resolution space. The former learns high-resolution features and fuses prior-guided low-resolution features to reconstruct clear images, while the latter utilizes normal and gradient priors to mine useful spatial features and detail features to guide high-resolution recovery better. To better utilize these priors, we introduce single prior feature interaction and dual prior feature interaction, where the former respectively fuses normal and gradient priors with high-resolution features to enhance prior ones, while the latter calculates the similarity between enhanced prior ones and further exploits dual guided filtering to boost the feature interaction of dual priors. We conduct experiments on both new and existing public datasets and demonstrate the state-of-the-art performance of our method on UHD image low-light enhancement, dehazing, deblurring, desnowing, and deraining. The source codes and benchmarks are available at <https://github.com/wlydlut/UHDDIP>.

Keywords Ultra-High-Definition image restoration · Ultra-High-Definition benchmarks · Dual interaction prior · Image desnowing · Image deraining

Liyan Wang
E-mail: wangliyan@mail.dlut.edu.cn

Cong Wang
E-mail: supercong94@gmail.com

Jinshan Pan
E-mail: sdluran@gmail.com

Xiaofeng Liu
E-mail: xiaofeng.liu@yale.edu

Weixiang Zhou
E-mail: s20201162006@mail.dlut.edu.cn

Xiaoran Sun
E-mail: sunxiaoran@mail.dlut.edu.cn

Wei Wang
E-mail: wangwei29@mail.sysu.edu.cn

Zhixun Su
E-mail: zxsu@dlut.edu.cn

¹ Dalian University of Technology, China

² Centre for Advances in Reliability and Safety, Hong Kong

³ Nanjing University of Science and Technology, China

⁴ Yale University, USA

⁵ Shenzhen Campus of Sun Yat-Sen University, China

⁶ Key Laboratory for Computational Mathematics and Data Intelligence of Liaoning Province, China

1 Introduction

Recently, as imaging and acquisition equipment developed by leaps and bounds, Ultra-High-Definition (UHD) images with high pixel density and high resolution (4K images containing 3840×2160 pixels) have continuously acquired attention. Compared with general images, UHD images naturally present more details and a wider color gamut, leaving continuous improvement of people's quality requirements for UHD images, which requires a systematic set of benchmark studies including the construction of relevant datasets and the design of algorithms suitable for processing

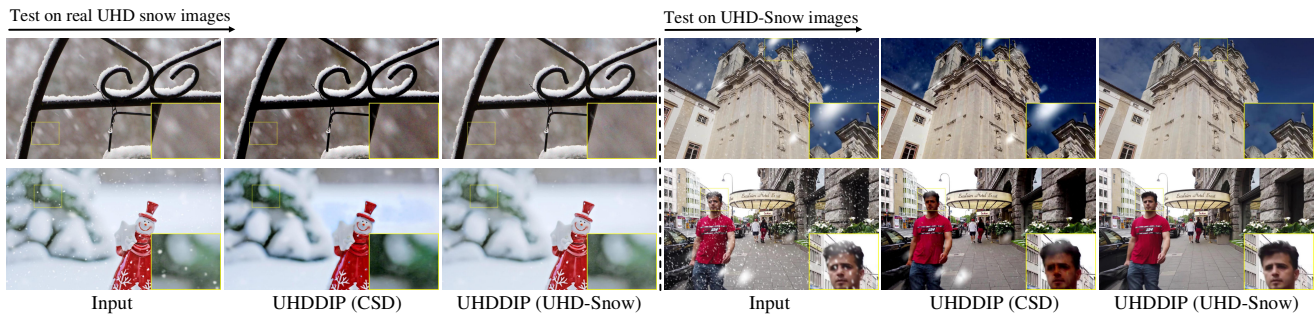


Fig. 1 The UHDDIP model, when trained on low-resolution desnowing datasets CSD (Chen et al., 2021b), fails to remove larger snowflakes and preserve the original image’s colors, while its performance remarkably improves after training on the proposed UHD-Snow dataset. Moreover, the visual results tested on the real UHD images (left three columns) and the proposed synthesized UHD-Snow images (right three columns) are consistent.

UHD restoration. Since current general learning-based image restoration algorithms (Wang et al., 2020b,a, 2021; Yao et al., 2021; Zhao et al., 2021; Chen et al., 2021c, 2020a; Zamir et al., 2021, 2022; Chen et al., 2021a; Tu et al., 2022; Wang et al., 2024a, 2022a, 2023a, 2024c; Mei et al., 2023; Zhang et al., 2022a) cannot effectively process UHD images (Li et al., 2023; Wang et al., 2024b), several UHD restoration models are developed (Zheng et al., 2021; Deng et al., 2021; Wang et al., 2023b; Li et al., 2023; Wang et al., 2024b) as well as UHD restoration benchmarks.

The specialized datasets for snow and rain UHD scenarios are largely unavailable at present, which hinders further exploration and research on the related tasks. If models are trained solely on previously synthesized low-resolution datasets, they exhibit significant shortcomings when applied to UHD images. For example, as illustrated in Fig. 1 (second column), training on the low-resolution desnowing dataset CSD (Chen et al., 2021b) results in difficulties removing larger snowflakes in real-world UHD snow images. Importantly, it tends to over-enhance, causing color inconsistencies with the original image. In contrast, training on the UHD dataset not only effectively removes snowflakes but also preserves the original image’s colors (Fig. 1, third column). Hence, constructing UHD snow and rain benchmarks is practically needed.

Recently, various approaches have been proposed for UHD restoration including multi-guided bilateral learning for UHD image dehazing (Zheng et al., 2021), multi-scale separable-patch integration networks for video deblurring (Deng et al., 2021), Transformer-based LLFormer (Wang et al., 2023b), Fourier embedding network UHDFour (Li et al., 2023) for UHD low-light image enhancement, and UHDformer (Wang et al., 2024b) by exploring the feature transformation from high- and low-resolution for UHD image restoration. However, these methods predominantly focus on the input image’s intrinsic features, not taking into

account additional relevant prior information conditions in model design, which makes it challenging to fully recover UHD images with more details and texture.

In this paper, we first construct two new benchmarks, named UHD-Snow and UHD-Rain, to facilitate the research of UHD image desnowing and deraining. Each dataset includes 3200 clean 4K images and corresponding degraded images synthesized by snowflakes and rain streaks with different densities, orientations, and locations, respectively. Among them, 3000 pairs are used for training and 200 pairs for testing. Fig. 2 shows some examples from UHD-Snow and UHD-Rain benchmarks. Furthermore, we propose an effective dual interaction prior-driven UHD restoration solution (UHDDIP). UHDDIP is built on two interesting observations: 1) the normal map contains shaped regions or boundaries of the texture that could provide more geometric spatial structures (e.g., Wang et al. (2024) utilize normal prior to mitigate texture interference.); 2) the gradient map reveals each local region’s edge and texture orientation that could render detail compensation. The interaction between normal and gradient priors allows for the synthesis of complementary information. Integrating these priors into model design will facilitate UHD restoration with finer structures and details. Based on these, we suggest the UHDDIP to solve UHD restoration problems effectively.

Specifically, UHDDIP contains two branches: (a) feature fusion and reconstruction branch in high-resolution space and (b) prior feature interaction branch in low-resolution space. The former learns high-resolution features and fuses prior-guided low-resolution features to reconstruct final clear images, while the latter explores prior feature interaction to render improved features with finer structures and detail features for high-resolution space. To better fuse and interact with prior features, we propose the prior feature interaction, containing single prior feature interaction (SPFI) and dual prior feature interaction (DPFI). The SPFI respectively

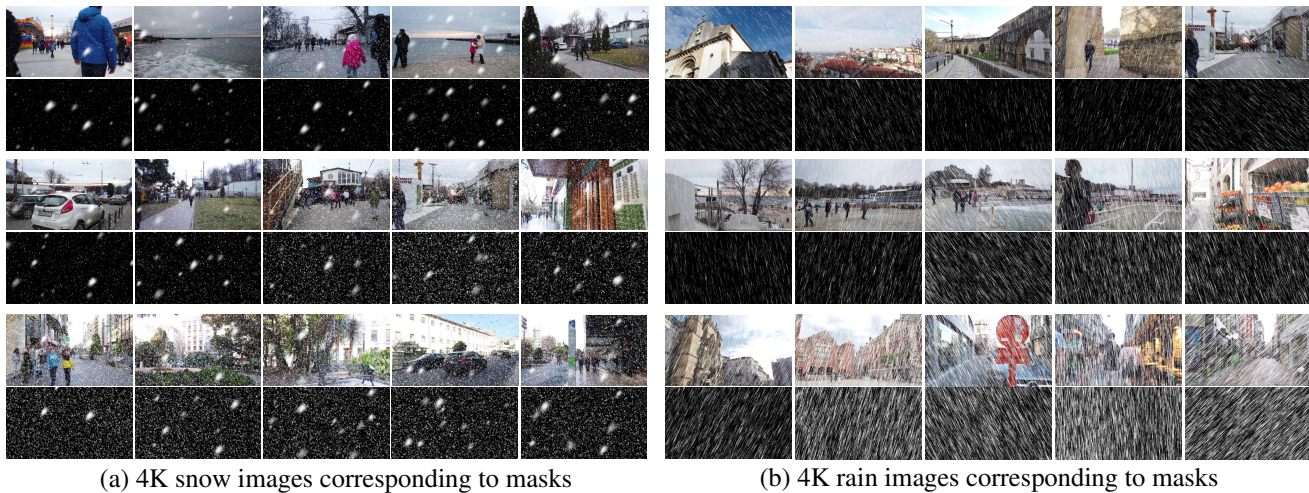


Fig. 2 The rain/snow images and their corresponding masks sampled from the proposed UHD-Snow and UHD-Rain datasets. Each dataset includes 3200 degraded/clean image pairs with 4K resolution (3000 pairs for training and 200 pairs for testing), which are synthesized snowflakes, snow streaks, and rain streaks with different densities, orientations, and locations.

fuses normal prior and gradient prior with high-resolution features to enhance prior ones, while the DPFI calculates the similarity between enhanced prior features and further exploits dual guided filtering to boost dual prior feature interaction for capturing better structures and details. Through interaction, these priors dynamically enhance each other’s strengths, leading to more robust features for guiding the high-resolution restoration. The main contributions are summarized as follows:

- We construct UHD-Snow and UHD-Rain benchmarks, each containing 3200 degraded/clean 4K image pairs, the first benchmarks used for UHD image desnowing and UHD image deraining so far as we know.
- We propose a general UHD image restoration framework, UHDDIP, which is built around a prior feature interaction module containing SPFI and DPFI, that incorporates gradient and normal priors into model design to achieve high-quality restoration with finer structures and details.
- Experiments on existing UHD datasets and established UHD-Snow and UHD-Rain benchmarks show that our method outperforms the state-of-the-art approaches on UHD low-light image enhancement, dehazing, deblurring, desnowing, and deraining.

2 Related Work

2.1 General Image Restoration

General Image Restoration (IR) aims to recover a clean image from its degraded observation, a task crucial in vari-

ous fields such as photography, medical imaging, and satellite imagery. Traditionally, IR methods have relied heavily on hand-crafted priors, including sparse coding (Luo et al., 2015), self-similarity (Buades et al., 2005), and gradient prior (Xu et al., 2013). However, they often falter when applied to real-world scenarios due to their limited robustness and generalization capabilities. The advent of deep learning marks a significant shift in the field, enabling the development of image restoration methods with the powerful implicit learning ability from large-scale data. By building various deep neural networks such as Convolutional Neural Network (CNN) (Krizhevsky et al., 2012; He et al., 2016), Residual Network (ResNet) (Zhang et al., 2021b), UNet (Zhang et al., 2022b), Transformer (Dosovitskiy et al., 2021), and have made extraordinary progress in the areas of image super-resolution (Dong et al., 2016), image deraining (Chen et al., 2023; Huang et al., 2021; Li et al., 2021), desnowing (Chen et al., 2021b, 2020b), deblurring (Lee and Cho, 2023; Wang et al., 2022b), dehazing (Song et al., 2023; Yang et al., 2013), denoising (Zhang et al., 2017; Zamir et al., 2022), etc. However, as models grow in complexity, there is a simultaneous increase in computational demands. Chen et al. (2022) propose NAFNet, a simple baseline that forgoes traditional activation functions and replaces the Transformer with plain block, achieving advanced performance with reduced complexity.

2.2 UHD Restoration Benchmarks

There have been several recent efforts to produce UHD datasets for specific image restoration tasks. For example, Zhang et al. (2021a) firstly provide two large-scale datasets, UHDSR4K and UHDSR8K collected from the Internet for

image super-resolution. UHDSR4K includes 8099 images with size of $3,840 \times 2,160$, and UHDSR8K includes 2966 images with size of $7,680 \times 4,320$. Zheng et al. (2021) create a 4K image dehazing dataset 4KID, which consists of 10,000 frames of hazy/sharp images extracted from 100 video clips by several different mobile phones. Based on UHDSR4K and UHDSR8K, Wang et al. (2023b) create the UHD-LOL by synthesizing corresponding low-light images. To process real low-light images with noise, Li et al. (2023) collect a real low-light image enhancement dataset UHD-LL, that contains 2,150 low-noise/normal-clear 4K image pairs captured in different scenarios. In addition, Deng et al. (2021) propose a 4KRD dataset comprised of blurry videos and corresponding sharp frames using three smartphones. To our knowledge, there are currently no UHD benchmark datasets specifically designed for UHD image desnowing and deraining. To address this gap, we construct two new benchmarks dedicated to UHD snow and rain scenarios.

2.3 UHD Image Restoration Approaches

Based on the above UHD benchmark datasets, a series of restoration works have made exciting progress in using deep learning-based approaches to recover clear UHD images. For example, Zheng et al. (2021) propose a multi-guided bilateral upsampling model for UHD image dehazing. To address the UHD video deblurring problem, Deng et al. (2021) develop a separable-patch integration network by working with a multi-scale integration scheme. Wang et al. (2023b) propose LLFormer, a transformer-based low-light image enhancement method, which is built by the axis-based multi-head self-attention and cross-layer attention fusion block. In contrast to the above approaches with UHD images in the spatial domain, Li et al. (2023) combine the Fourier transform into low-light image enhancement by utilizing amplitude and phase in a cascade network. However, the above methods usually rely on large-capacity models for optimal performance, and the recovered results are often unsatisfactory. Wang et al. (2024b) propose a small-capacity model, UHDformer, to solve the UHD image restoration problem, which demonstrates excellent performance on three tasks, by exploring the feature transformation from high- and low-resolution for UHD image restoration. In contrast to existing methods that focus solely on extracting features from the input image itself and do not yet explore other related prior information, we propose a dual interaction prior-driven UHD image restoration framework, which innovatively integrates additional priori information and mines more robust features to facilitate restoration.

3 UHD-Snow and UHD-Rain Datasets

We first introduce the source and construction of proposed UHD-Snow and UHD-Rain datasets in Sec. 3.1. Next, the

mask generation process for UHD rain and snow is provided in Sec. 3.2.

3.1 Source and Construction

We construct two UHD-Snow and UHD-Rain datasets composed of 4K images of $3,840 \times 2,160$ resolution based on large-scale image datasets UHDSR4K (Zhang et al., 2021a). In detail, we extract 3200 original UHD images from the UHDSR4K dataset used for UHD image super-resolution to synthesize corresponding rain and snow images following Photoshop’s rain and snow synthesis tutorial. UHDSR4K provides 8099 images of $3,840 \times 2,160$ resolution collected from the Internet (Google, Youtube, and Instagram) containing diverse scenes such as city scenes, people, animals, buildings, cars, natural landscapes, and sculptures. The training set is constructed by selecting the first 2,800 images from the training set and the first 200 images from the testing set in UHDSR4K (excluding indoor images), ensuring continuity with several adjacent images depicting the same scene. The testing set comprises 200 images randomly chosen from various scenes within the testing set of UHDSR4K, excluding the initial 200 images already utilized in the training set.

Based on the UHDSR4K dataset, we synthesize snowflakes and snow streaks with different sizes and densities following the snow mask of CSD (Chen et al., 2021b) and rainy streaks with different densities and orientations following the rain mask of Rain100L (Yang et al., 2020) and Rain100H (Yang et al., 2017). Finally, the snow and rain masks are added to the corresponding UHD clean images to synthesize our UHD-Snow and UHD-Rain, which contain 3000 pairs for training and 200 pairs for testing, respectively. The statistics of our UHD datasets are summarized in Fig. 3.

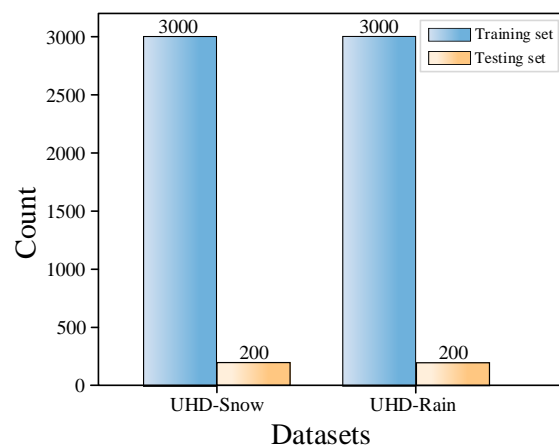


Fig. 3 Statistics of our constructed UHD-Snow and UHD-Rain benchmarks.

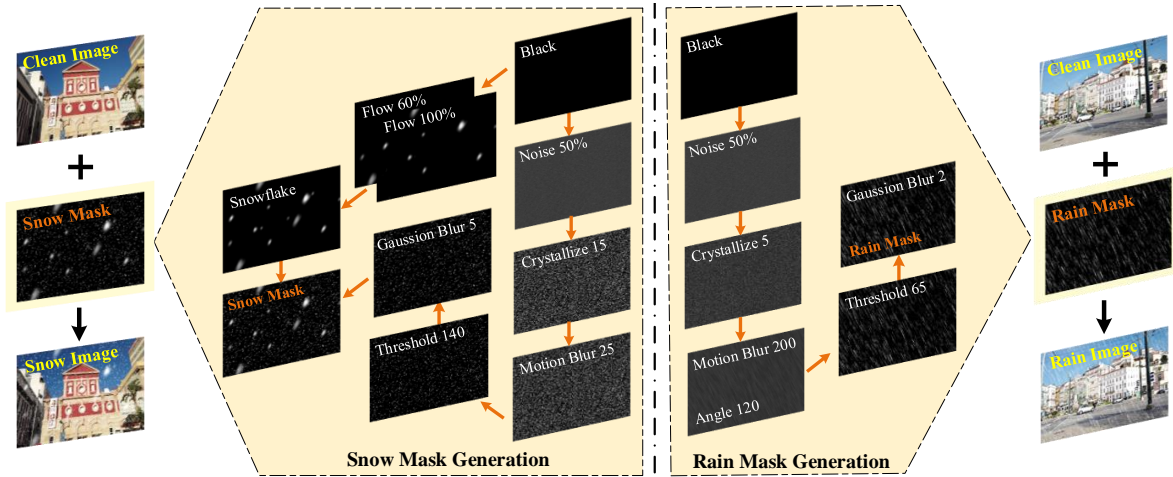


Fig. 4 The flowchart of snow (left) and rain (right) mask generation. In the snow mask generation process, we set the parameters as follows: 50% noise (amount), 15 crystallize (cell size), 25 pixels motion blur (distance), a threshold level range of 100-165 to control the density of the snow streaks, 5 pixels Gaussian blur (radius), and two flows of 60% and 100% to create snowflakes with varying transparency. For the generation of rain mask, the parameters are set: 50% noise, 5 crystallize, 200 pixels motion blur with an angle range of 45° - 135° , a threshold level range of 55-67, and 2 pixels Gaussian blur.

Table 1 Photoshop’s parameter settings for mask generation (50 different angles with a range of 45° - 135° include $45^\circ, 50^\circ, 55^\circ, 60^\circ$ - $80^\circ, 85^\circ, 95^\circ, 100^\circ$ - $120^\circ, 125^\circ, 130^\circ, 135^\circ$).

Datasets	Noise	Crystallize	Motion Blur	Gaussian Blur	Threshold	Angle	Flow
UHD-Snow	50%	15	25	5	100-165	-	60%, 100%
UHD-Rain	50%	5	200	2	55-67	45° - 135°	-

3.2 Mask Generation

For the training set, we create 600 different UHD snow and rain masks. Among them, the snow masks contain snow streaks with 10 different densities and snowflakes with different sizes, and the rain masks contain rain streaks with 50 different orientations and 4 different densities, which ensures the diversity of the generation. Furthermore, we adopt the Gaussian blur on rain particles and snow particles to better simulate real-world rain and snow scenarios. We apply the same manner to the testing set to recreate 200 different UHD snow and rain masks. Note that UHD-Snow and UHD-Rain datasets share the same clean images, which ensures that differences in model performance are due to weather effects rather than scene variation.

In the synthesis process, we first randomly generate noise and then apply crystallization, motion blur, Gaussian blur, threshold adjustment, etc. For the snow mask, we set the parameters as follows: 50% noise (amount), 15 crystallize (cell size), 25 pixels motion blur (distance), 5 pixels Gaussian blur (radius), and a threshold level range of 100-165 to control the density of the snow streaks. Additionally, we adopt two flows of 60% and 100% to create snowflakes

with varying transparency. For the rain mask, the parameters are set as follows: 50% noise, 5 crystallize, 200 pixels motion blur, 2 pixels Gaussian blur, and a threshold level range of 55-67 to control the density of the rain streaks. We then apply motion blur with an angle range of 45° - 135° . Detailed parameter settings are shown in Table 1. The flowchart illustrating the mask generation for our UHD-Snow and UHD-Rain datasets is depicted in Fig. 4.

4 Overview of UHDDIP

Fig. 5 depicts our proposed UHDDIP, containing two branches: (a) feature fusion and reconstruction branch in high-resolution space, which fuses low-resolution features into the high-resolution space and reconstructs final latent clean images; (b) prior feature interaction branch in the low-resolution space to modulate normal and gradient priors into useful features to guide high-resolution learning.

4.1 Feature Fusion and Reconstruction Branch in High-Resolution Space

As depicted in Fig. 5(a), given a degraded UHD image $U \in \mathbb{R}^{H \times W \times 3}$ as input, UHDDIP firstly applies a 3×3 con-

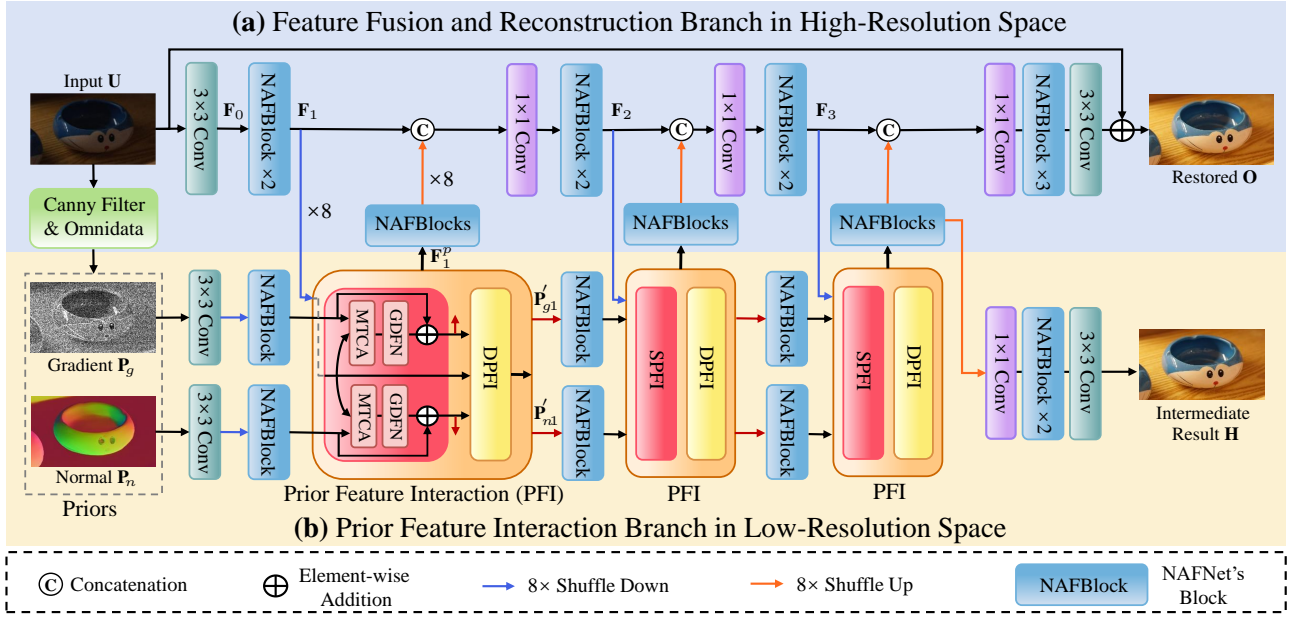


Fig. 5 Overview of our Dual Interaction Prior-driven UHD restoration network (UHDDIP). UHDDIP contains two branches: (a) feature fusion and reconstruction branch in high-resolution space, which fuses low-resolution features into high-resolution space and reconstructs final images; (b) prior feature interaction branch in low-resolution space to modulate normal and gradient prior into useful features to guide high-resolution learning. We utilize NAFBlock (Chen et al., 2022) as basic feature learning units.

volution layer to extract shallow feature $\mathbf{F}_0 \in \mathbb{R}^{H \times W \times C}$, where $H \times W$ denotes the spatial dimension and C is the number of channels. Next, \mathbf{F}_0 is fed into the first group of NAFBlocks to obtain the first-level high-resolution feature \mathbf{F}_1 . Then, \mathbf{F}_1 is passed by $8 \times$ shuffled-down into the low-resolution space to produce \mathbf{F}_1^p that interacts with the prior features, and then \mathbf{F}_1^p is fed into NAFBlocks for further learning. The output features are $8 \times$ shuffled-up to be concatenated with the first-level high-resolution feature \mathbf{F}_1 at channel dimension and a new first-level feature \mathbf{F}'_1 is obtained after a 1×1 convolution. Then, the fused feature \mathbf{F}'_1 is fed into the second group NAFBlocks and the same action continues to be performed until after the third group NAFBlocks, high-resolution feature reconstruction starts to be implemented. Finally, the output generated after three NAFBlocks and a 3×3 convolutional layer is added to the input image to obtain the final restored image $\mathbf{O} \in \mathbb{R}^{H \times W \times 3}$.

4.2 Prior Feature Interaction Branch in Low-Resolution Space

To provide richer structures and details, we respectively operate on the input image \mathbf{U} using the Omnidata (Eftekhari et al., 2021) and the Canny filter to generate normal prior $\mathbf{P}_n \in \mathbb{R}^{H \times W \times 3}$ and gradient prior $\mathbf{P}_g \in \mathbb{R}^{H \times W \times 1}$. As shown in Fig. 5(b), in the low-resolution space, \mathbf{P}_n and \mathbf{P}_g

are first fed into a 3×3 convolution and the first NAFBlock, to produce the first-level prior features \mathbf{P}_{n1} and \mathbf{P}_{g1} , which serve as the input of the first prior feature interaction (PFI) module. At the same time, PFI also receives \mathbf{F}_1 passed down from the high-resolution and encodes and interacts it along with \mathbf{P}_{n1} and \mathbf{P}_{g1} to generate interacted low-resolution feature \mathbf{F}'_1 , and enhanced prior features \mathbf{P}'_{n1} , \mathbf{P}'_{g1} that are fed into the second PFI to continue performing the same actions. Until \mathbf{P}'_{ni} and \mathbf{P}'_{gi} and \mathbf{F}'_i are obtained after the output of the i^{th} ($i = 1, \dots, L$) PFI, these features are aggregated into the high-resolution branch to participate in the reconstruction of the final image. Moreover, the result \mathbf{H} generated after two NAFBlocks and a 3×3 convolutional layer is further used to supervise the low-resolution branch.

4.3 Prior Feature Interaction

PFI contains two sub-modules: Single Prior Feature Interaction (SPFI) and Dual Prior Feature Interaction (DPFI). The SPFI respectively fuses normal prior and gradient prior with high-resolution features to enhance prior ones, while the DPFI calculates the similarity between enhanced prior features and further exploits dual guided filtering to boost dual prior feature interaction.

Single Prior Feature Interaction. The main challenge

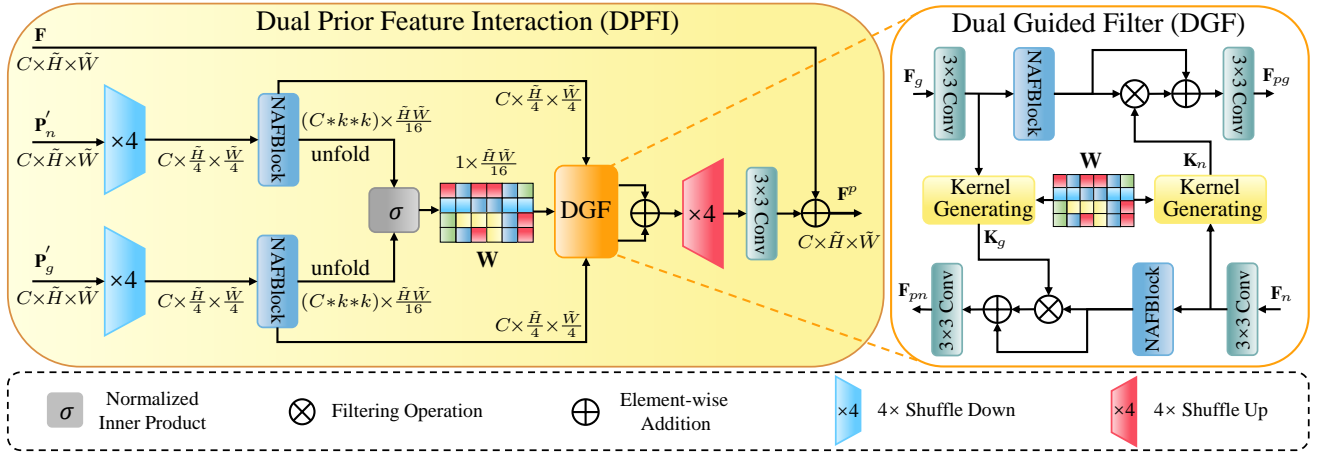


Fig. 6 Dual Prior Feature Interaction (DPFI). DPFI aims to compute the similarity between two enhanced single prior features by employing their intrinsic properties to form interacted prior features, which provides meaningful guidance for feature learning in high-resolution space.

of utilizing normal and gradient priors guides the image restoration lies in how to enable the network to be aware of image details and structure at the pixel level effectively. To this end, we employ SPFI to enhance single prior features. As shown in Fig. 7(a) and Fig. 7(e), we extract the features of the normal and gradient priors before entering the first SPFI, respectively. Intuitively, normal features naturally provide the finer geometrical structure (arm’s boundaries in the yellow box), while gradient features contain more texture details (letters in the blue box), and they can provide complementary information. These features, respectively, are integrated with high-resolution features by the SPFI module to further enhance corresponding structures and details (See Fig. 7(b) and Fig. 7(f)).

Specifically, in SPFI, \mathbf{P}_{ni} and \mathbf{P}_{gi} are respectively fused with \mathbf{F}_i through two groups of Multi-Dconv Head Transposition Cross Attention (MTCA), which is defined as (For simplicity, we denote \mathbf{P}_{ni} , \mathbf{P}_{gi} , \mathbf{F}_i below as \mathbf{P}_n , \mathbf{P}_g , \mathbf{F}):

$$MTCA(\mathbf{Q}_p^n, \mathbf{K}_f, \mathbf{V}_f) = \text{Softmax}(\mathbf{Q}_p^n \mathbf{K}_f^T / \sqrt{f_k}) \mathbf{V}_f, \quad (1)$$

$$MTCA(\mathbf{Q}_p^g, \mathbf{K}_f, \mathbf{V}_f) = \text{Softmax}(\mathbf{Q}_p^g \mathbf{K}_f^T / \sqrt{f_k}) \mathbf{V}_f, \quad (2)$$

where the query \mathbf{Q}_p^n is derived from normal prior feature \mathbf{P}_n ; \mathbf{Q}_p^g is derived from grad prior feature \mathbf{P}_g ; the key \mathbf{K}_f and value \mathbf{V}_f are derived from image feature \mathbf{F} . These matrices are generated through layer normalization, 1×1 convolutions, and 3×3 depth-wise convolutions as orders.

Then, we employ the Gated-Dconv Feed-forward Network (GDFN) (Zamir et al., 2022) to generate single prior features \mathbf{P}'_n and \mathbf{P}'_g based on the attention map and the original prior features:

$$\mathbf{P}'_n = GDFN(\mathbf{P}_n + MTCA(\mathbf{Q}_p^n, \mathbf{K}_f, \mathbf{V}_f)), \quad (3)$$

$$\mathbf{P}'_g = GDFN(\mathbf{P}_g + MTCA(\mathbf{Q}_p^g, \mathbf{K}_f, \mathbf{V}_f)), \quad (4)$$

Finally, \mathbf{P}'_n and \mathbf{P}'_g , as enhanced prior features of the current stage, are fed into the subsequent DPFI to implement the dual prior feature interaction and are also passed to the next SPFI to learn further.

Dual Prior Feature Interaction. DPFI aims to compute the similarity between two enhanced single priors by employing their intrinsic properties to further capture image structures and details, which provides meaningful guidance for high-resolution space. As shown in Fig. 6, we first down-sample features $\mathbf{P}'_n \in \mathbb{R}^{C \times \tilde{H} \times \tilde{W}}$ ($\tilde{H} = H/8, \tilde{W} = W/8$) and $\mathbf{P}'_g \in \mathbb{R}^{C \times \tilde{H} \times \tilde{W}}$ by a factor of 4 to reduce the subsequent computational burden. They are then unfolded by a $k * k$ kernel ($k = 3$) after passing through the NAFBlock in parallel, yielding patches of size $(C * k * k) \times \tilde{H}\tilde{W}/16$. We compute all patches similarity using normalized inner product (Lu et al., 2021), and further obtain similarity weight $\mathbf{W} \in [1 \times \tilde{H}\tilde{W}/16]$. Motivated by (Wang et al., 2024), we apply two prior features and similarity weight to the Dual Guided Filter (DGF) to further filter out irrelevant features while balancing the structure and detail.

Specifically, DGF accepts two prior features $\mathbf{F}_n, \mathbf{F}_g$ and similarity weights \mathbf{W} as inputs and then generates the normal prior filter kernel and the gradient prior filter kernel, denoted as $\mathbf{K}_n, \mathbf{K}_g$:

$$\mathbf{K}_n = g(\text{Conv}_3(\mathbf{F}_n), \mathbf{W}), \mathbf{K}_g = g(\text{Conv}_3(\mathbf{F}_g), \mathbf{W}), \quad (5)$$

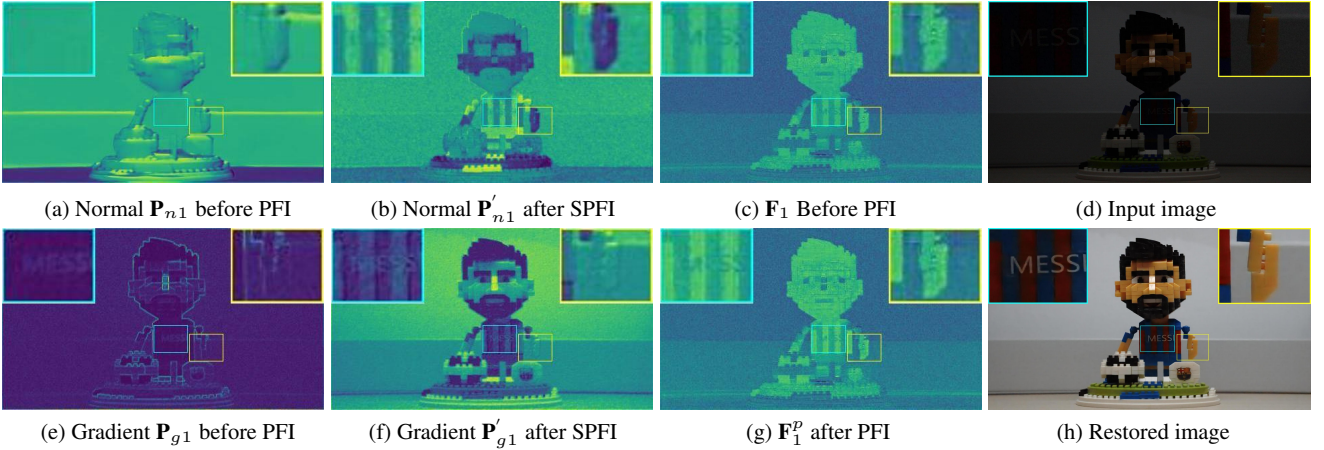


Fig. 7 Feature visualization at the first SPFI and DPFI module. The normal prior feature (a) contains better structures, while the gradient prior feature (e) possesses richer details. Compared to without prior features (c), using normal prior alone (b) helps to enhance the geometric structure of the image, like the arm’s boundaries. Applying only gradient prior (f) can improve finer texture details, like the letters’ clarity. Whereas, utilizing in conjunction (g) performs the best. Through interaction, two priors dynamically enhance each other’s strengths, to produce a result with finer structures and richer textures.

where g denotes kernel generating module, containing a 1×1 convolution and an activation function.

Then, the two kernels filter the two prior features separately to preserve their respective prior attributes and further filter out irrelevant features:

$$\mathbf{F}_{pn} = \mathbf{F}_n \otimes \mathbf{K}_g + \mathbf{F}_n, \quad \mathbf{F}_{pg} = \mathbf{F}_g \otimes \mathbf{K}_n + \mathbf{F}_g, \quad (6)$$

where \otimes is the filtering operation; note that here \mathbf{F}_n and \mathbf{F}_g are obtained after a 3×3 convolution and a NAFBlock. Finally, prior features are added to the low-resolution features passed down from the high-resolution to produce an interacted prior feature \mathbf{F}^p .

Fig. 7(g) presents visualization features in the first PFI. One can observe that PFI can effectively improve both structure and detail features, which further facilitates restoration.

4.4 Loss Function

Following UHDformer (Wang et al., 2024b), we optimize our UHDDIP by minimizing the L_1 loss and frequency loss (Cho et al., 2021) between the restored result \mathbf{O} , intermediate result \mathbf{H} and ground truth \mathbf{G} :

$$\begin{aligned} \mathcal{L}_{\text{total}} = & \|\mathbf{O} - \mathbf{G}\|_1 + \lambda \|\mathcal{F}(\mathbf{O}) - \mathcal{F}(\mathbf{G})\|_1 \\ & + \alpha \|\mathbf{H} - \mathbf{G}\|_1 + \lambda \|\mathcal{F}(\mathbf{H}) - \mathcal{F}(\mathbf{G})\|_1, \end{aligned} \quad (7)$$

where $\|\cdot\|_1$ denotes L_1 norm; \mathcal{F} denotes the Fast Fourier transform; α and λ are weights that are empirically set to 0.5 and 0.1.

5 Experiment

We present performance comparisons with state-of-the-art approaches on 5 UHD image restoration tasks, including (a) low-light enhancement, (b) dehazing, (c) deblurring, (d) desnowing, and (e) deraining.

5.1 Experimental Setup

Implementation Details. We incorporate 3 PFI modules in low-resolution space for the network setting based on NAFBlocks (total 29 in this paper) backbones, and 4 NAFBlocks follow each PFI. The number of attention heads in MTCA is set to 8, and the number of channels is 16. We train models using AdamW optimizer with the initial learning rate $5e^{-4}$ gradually reduced to $1e^{-7}$ with the cosine annealing (Loshchilov and Hutter, 2017). The model is trained with a total batch size of 12 on two NVIDIA RTX A6000 GPUs. During training, we utilize cropped patches with a size of 512×512 for 60K iterations in low-light image enhancement, 500K iterations in desnowing, deraining, and dehazing, and 600K iterations in deblurring.

Datasets. We use the UHD-LL (Li et al., 2023), UHD-Blur (Wang et al., 2024b), and UHD-Haze (Wang et al., 2024b) in line with previous works (Li et al., 2023; Wang et al., 2024b) as the UHD low-light image enhancement, deblurring, and dehazing benchmarks, respectively. For UHD image desnowing and deraining, we use our proposed UHD-Snow and UHD-Rain datasets to evaluate the desnowing and deraining performance, respectively.

Table 2 Low-light image enhancement on UHD-LL dataset. General and UHD respectively denote the general and UHD image restoration methods. The best and second best are marked in **bold** and underlined, respectively. $\uparrow(\downarrow)$ means higher(lower) is better.

Type	Methods	Venue	PSNR \uparrow	SSIM \uparrow	LPIPS \downarrow
General	SwinIR (Liang et al., 2021)	ICCVW'21	21.165	0.8450	0.3995
	Restormer (Zamir et al., 2022)	CVPR'22	21.536	0.8437	0.3608
	Uformer (Wang et al., 2022b)	CVPR'22	21.303	0.8233	0.4013
UHD	LLFormer (Wang et al., 2023b)	AAAI'23	24.065	0.8580	0.3516
	UHDFour (Li et al., 2023)	ICLR'23	26.226	0.9000	0.2390
	UHDformer (Wang et al., 2024b)	AAAI'24	27.113	<u>0.9271</u>	<u>0.2240</u>
	UHDDIP (Ours)	-	<u>26.749</u>	0.9281	0.2076

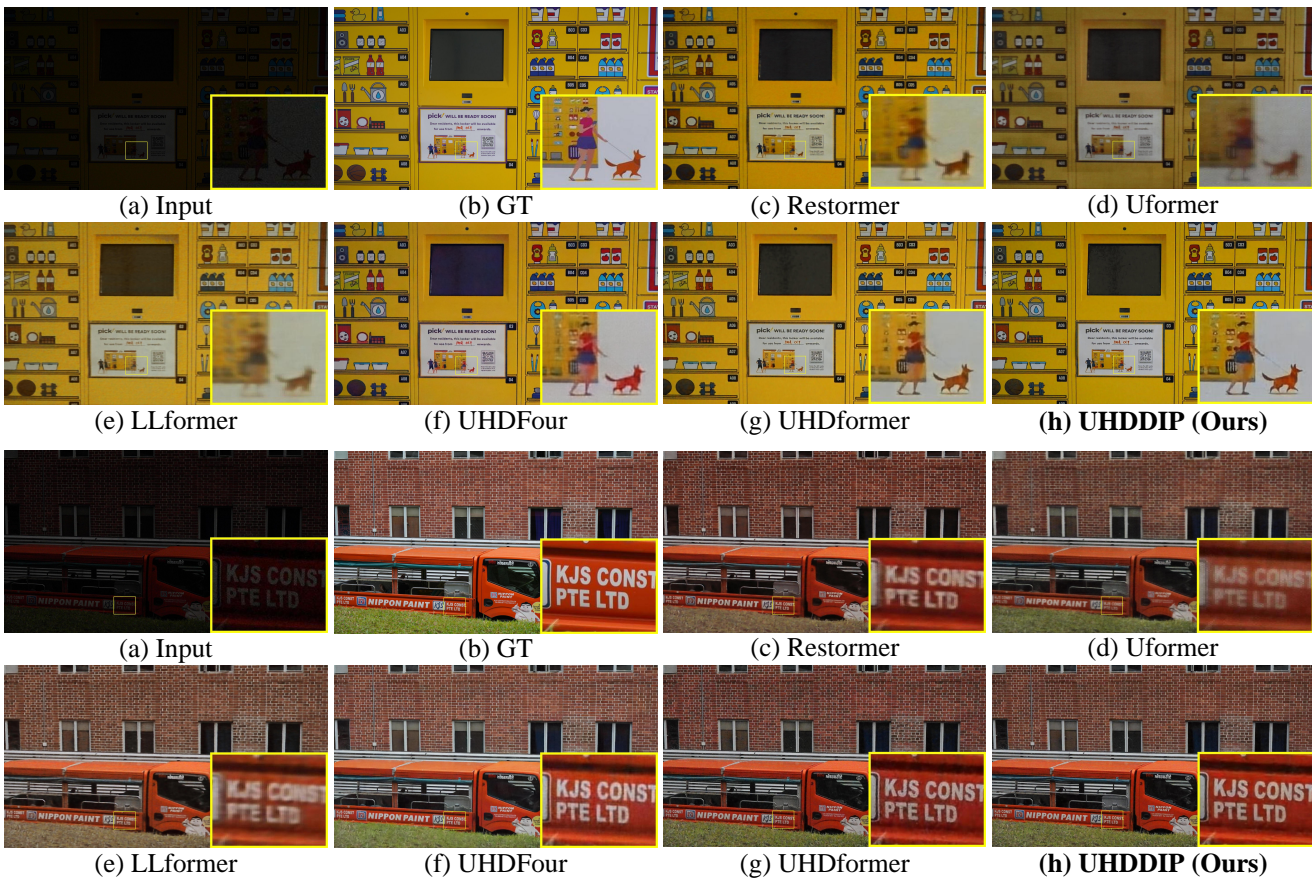


Fig. 8 Low-light image enhancement on UHD-LL. Our UHDDIP can generate clearer results.

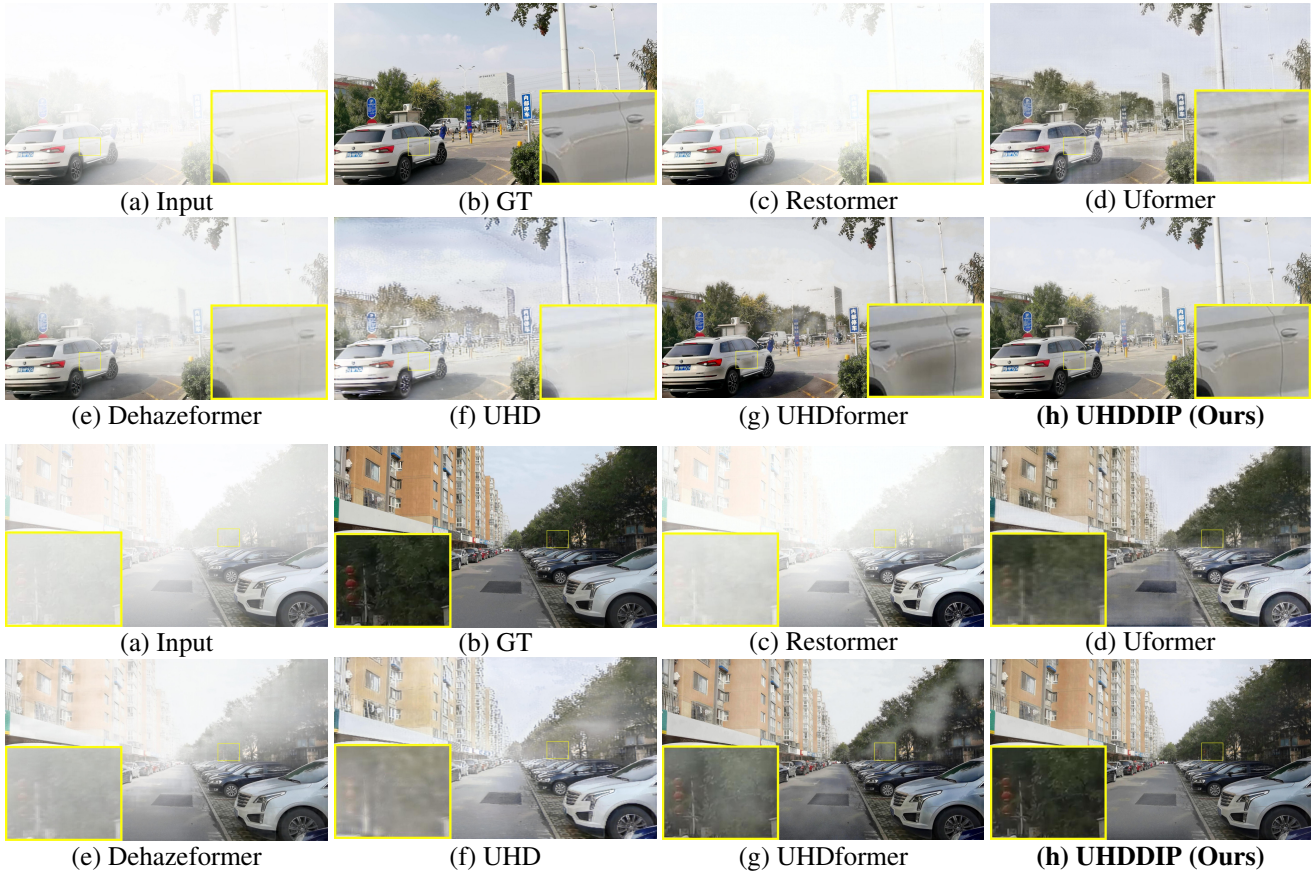
Evaluation Metrics. We quantitatively measure restored performance by reporting the PSNR (Huynh-Thu and Ghanbari, 2008), SSIM (Wang et al., 2004), and LPIPS (Zhang et al., 2018) of all compared methods. Following (Li et al., 2023; Wang et al., 2024b), for methods that cannot directly process full-resolution UHD images, we resize the input image to the maximum size the model can handle and return to the original size after testing.

Compared Methods. We adopt seven general IR methods such as SwinIR (Liang et al., 2021), Uformer (Wang

et al., 2022b), Restormer (Zamir et al., 2022), DehazeFormer (Song et al., 2023), Stripformer (Tsai et al., 2022), FFTformer (Kong et al., 2023), and SFNet (Wang et al., 2024), and four UHD IR methods (i.e., LLFormer (Wang et al., 2023b), UHDFour (Li et al., 2023), UHD (Zheng et al., 2021), and UHDformer (Wang et al., 2024b)) as benchmarks. For a fair comparison, we retrain the models according to the officially released codes of these methods and use the weights with the same number of iterations as our method for testing purposes.

Table 3 Image dehazing on the UHD-Haze dataset. The best and second best are marked in **bold** and underlined.

Type	Methods	Venue	PSNR \uparrow	SSIM \uparrow	LPIPS \downarrow
General	Restormer (Zamir et al., 2022)	CVPR'22	12.718	0.6930	0.4560
	Uformer (Wang et al., 2022b)	CVPR'22	19.828	0.7374	0.4220
	DehazeFormer (Song et al., 2023)	TIP'23	15.372	0.7045	0.3998
UHD	UHD (Zheng et al., 2021)	ICCV'21	18.048	0.8113	0.3593
	UHDformer (Wang et al., 2024b)	AAAI'24	<u>22.586</u>	<u>0.9427</u>	<u>0.1188</u>
	UHDDIP (Ours)	-	24.699	0.9520	0.1049

**Fig. 9** Image dehazing on UHD-Haze. Our UHDDIP is capable of producing clearer results.

5.2 Main Results

UHD Low-Light Image Enhancement. In line with previous work (Li et al., 2023; Wang et al., 2024b), we evaluate the UHD low-light image enhancement on UHD-LL (Li et al., 2023) as summarized in Table 2. Despite a slight inferiority in PSNR in comparison to UHDformer (Wang et al., 2024b), our method outperforms UHDformer in terms of SSIM and LPIPS. It is clearly witnessed that our UHDDIP can obtain excellent perceptual quality. Fig. 8 presents a visual comparison, where UHDDIP can generate a clearer structure and more natural color.

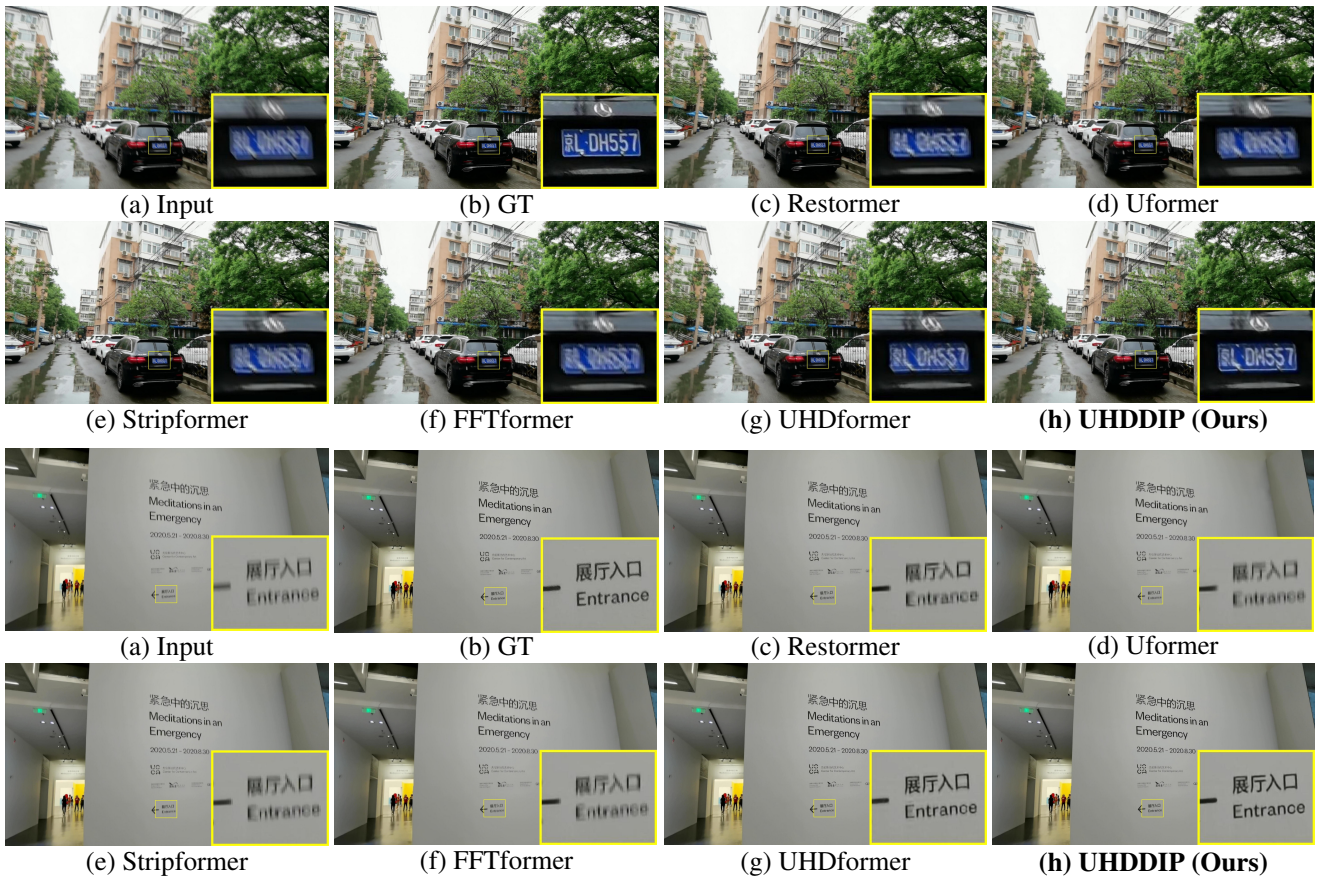
UHD Image Dehazing. Table 3 shows the evaluation

of our UHDDIP and other dehazing methods on the UHD-Haze testing set. Our UHDDIP consistently outperforms general and UHD IR methods. Compared to UHDformer (Wang et al., 2024b), our method achieves a substantial gain of 2.113dB PSNR. We provide visual examples in Fig. 9 for UHD dehazing. It can be seen that our UHDDIP is effective in removing haze and restoring images that are visually closer to the ground truth than those of the other approaches. However, UHDformer (Wang et al., 2024b) can tend to over-defog, resulting in a noticeable loss of detail.

UHD Image Deblurring. Table 4 compares UHDDIP with the general IR method and UHD IR backbone

Table 4 Image deblurring on the UHD-Blur dataset. The best and second best are marked in **bold** and underlined.

Type	Methods	Venue	PSNR \uparrow	SSIM \uparrow	LPIPS \downarrow
General	Restormer (Zamir et al., 2022)	CVPR'22	25.210	0.7522	0.3695
	Uformer (Wang et al., 2022b)	CVPR'22	25.267	0.7515	0.3851
	Stripformer (Tsai et al., 2022)	ECCV'22	25.052	0.7501	0.3740
	FFTformer (Kong et al., 2023)	CVPR'23	25.409	0.7571	0.3708
UHD	UHDformer (Wang et al., 2024b)	AAAI'24	<u>28.821</u>	<u>0.8440</u>	<u>0.2350</u>
	UHDDIP (Ours)	-	29.517	0.8585	0.2127

**Fig. 10** Image deblurring on UHD-Blur. Our UHDDIP is capable of producing clearer results.

networks on the UHD-Blur testing set, our UHDDIP demonstrates superior performance. For example, compared to UHD methods, UHDDIP is 0.696dB in terms of PSNR higher than UHDformer (Wang et al., 2024b). In addition, UHDDIP outperforms the general methods by considerable margins in terms of PSNR, SSIM, and LPIPS. A visual comparison of UHDDIP with other approaches is also illustrated in Fig. 10. Our method produces mostly clear visual results and is closer to the ground truth.

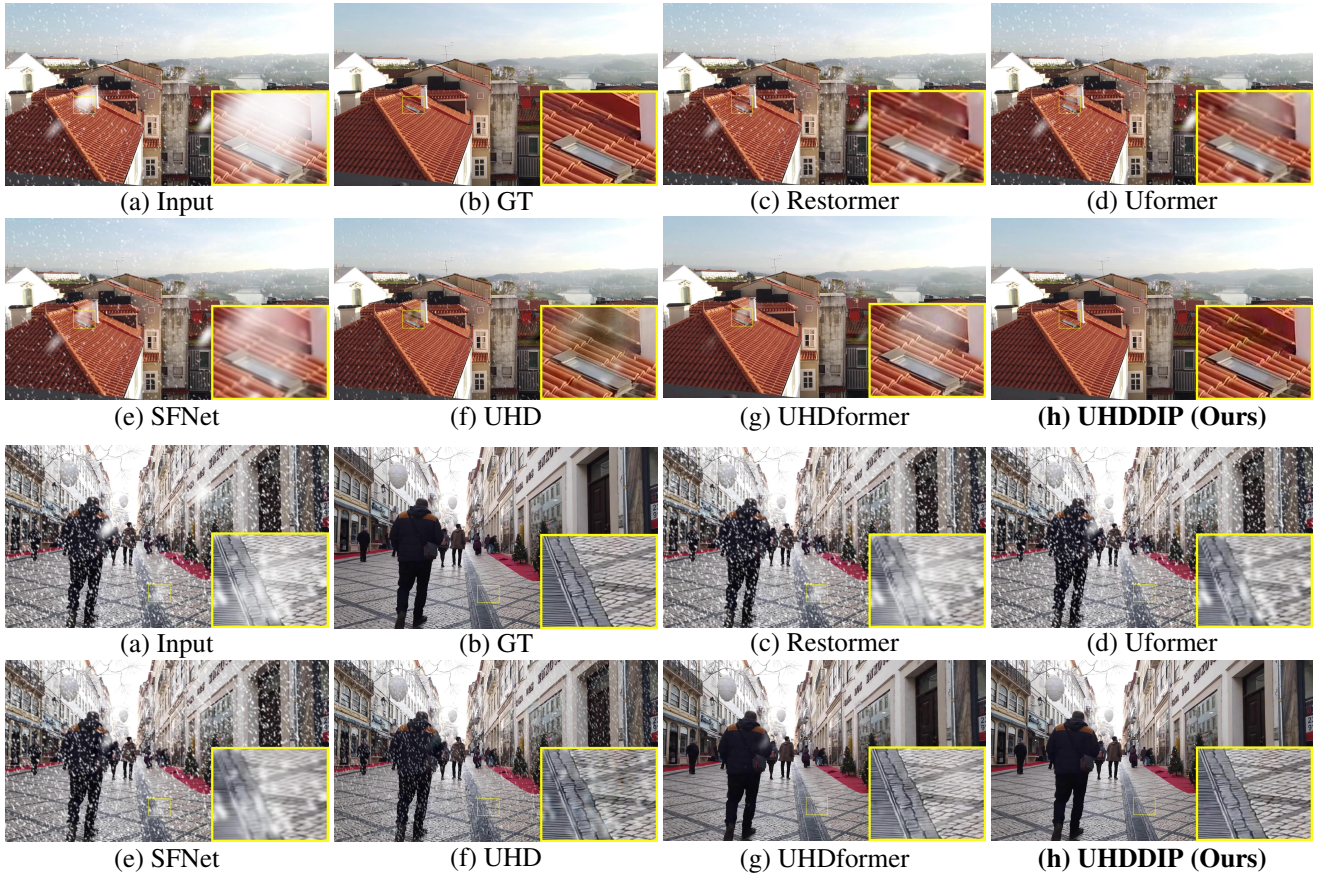
UHD Image Desnowing. We implement UHD desnowing experiment on the constructed UHD-Snow dataset. Table 5 summarizes the quantitative results. One can obviously

observe that UHDDIP achieves the best performance. Our UHDDIP yields a 4.949dB PSNR performance gain over the previous best method UHDformer (Wang et al., 2024b). Fig. 11 shows that UHDDIP effectively removes snow and produces a clearer structure while preserving more details.

UHD Image Deraining. We evaluate UHD image deraining with the constructed UHD-Rain dataset. The results are reported in Table 6. As one can see UHDDIP significantly advances current state-of-the-art approaches. Especially, our UHDDIP achieves a substantial gain of 2.828dB PSNR compared to UHDformer (Wang et al., 2024b). Fig. 12 shows our UHDDIP effectively removes

Table 5 Image desnowing on the UHD-Snow dataset. The best and second best are marked in **bold** and underlined.

Type	Methods	Venue	PSNR \uparrow	SSIM \uparrow	LPIPS \downarrow
General	Uformer (Wang et al., 2022b)	CVPR'22	23.717	0.8711	0.3095
	Restormer (Zamir et al., 2022)	CVPR'22	24.142	0.8691	0.3190
	SFNet (Cui et al., 2023)	ICLR'23	23.638	0.8456	0.3528
UHD	UHD (Zheng et al., 2021)	ICCV'21	29.294	0.9497	0.1416
	UHDformer (Wang et al., 2024b)	AAAI'24	<u>36.614</u>	<u>0.9881</u>	<u>0.0245</u>
	UHDDIP (Ours)	-	41.563	0.9909	0.0179

**Fig. 11** Image desnowing on UHD-Snow. Our UHDDIP is able to generate clearer results.

rain streaks and generates visually pleasant rain-free images, whereas existing methods often struggle to restore UHD images well.

5.3 Ablation Study

We conduct the ablation study to analyze the effect of each component on 3 UHD IR tasks including low-light image enhancement, deraining, and desnowing, and all models are trained on a patch of size 512×512 for 60K iterations.

Effect of Prior Feature Interaction. Since the prior feature interaction module plays one important role in our

model, we investigate its effect on UHD low-light image enhancement, desnowing, and deraining in Table 7(a), (c), and (e), respectively. We note that removing the PFI leads to a noticeable performance drop in all metrics on 3 tasks. For the UHD low-light image enhancement, only using the SPFI module degrades the network's performance, while DPFI contributes to performance improvement. Whereas, utilizing in conjunction performs the best, and our method surpasses the baseline by 0.25dB PSNR. Furthermore, it can be discovered that our SPFI and DPFI modules both play an important role in desnowing and deraining tasks. Fig. 13 presents the visual comparison of 3 tasks, where our full model is able to generate results with clearer structures

Table 6 Image deraining on the UHD-Rain dataset. The best and second best are marked in **bold** and underlined.

Type	Methods	Venue	PSNR \uparrow	SSIM \uparrow	LPIPS \downarrow
General	Uformer (Wang et al., 2022b)	CVPR'22	19.494	0.7163	0.4598
	Restormer (Zamir et al., 2022)	CVPR'22	19.408	0.7105	0.4775
	SFNet (Cui et al., 2023)	ICLR'23	20.091	0.7092	0.4768
UHD	UHD (Zheng et al., 2021)	ICCV'21	26.183	0.8633	0.2885
	UHDformer (Wang et al., 2024b)	AAAI'24	<u>37.348</u>	<u>0.9748</u>	<u>0.0554</u>
	UHDDIP (Ours)	-	40.176	0.9821	0.0300

**Fig. 12** Image deraining on UHD-Rain. Our UHDDIP is capable of producing clearer results.

and more natural colors.

Effect of Priors. Table 7(b), (d), and (f) report the effect of the priors on 3 tasks, respectively. We find that for UHD low-light image enhancement, the normal prior contributes to the improvement of SSIM and LPIPS compared without using any priors, while the gradient prior helps yield the optimal PSNR. When both, our method achieves the best performance in terms of SSIM and LPIPS. On the other hand, for desnowing and deraining, both normal and gradient priors contribute to improved restoration quality. The analysis indicates that considering gradient and normal priors in model design may benefit

tasks like desnowing/deraining that focus on preserving and enhancing details and structures. However, it may introduce noise in low-light image enhancement, resulting in lower PSNR and higher SSIM values. Fig. 14 illustrates a visual comparison on UHD low-light image enhancement. We observe that normal and gradient priors produce distinct structures and details (See (b) and (g) in Fig. 14). When combined, our method produces sharper structures and richer details.

5.4 Additional Experiments

We conduct additional experiments to discuss the effect of each component used in our UHDDIP framework, including

Table 7 Ablation study. Each component in Prior Feature Interaction (PFI) is effective and each prior used in our model can enhance recovery quality.

(a) Effect of PFI on UHD low-light image enhancement.

Module	PSNR \uparrow	SSIM \uparrow	LPIPS \downarrow
w/o PFI	26.499	0.9269	0.2169
w/o DPFI	26.226	0.9232	0.2179
w/o SPFI	26.557	0.9259	0.2171
Full (Ours)	26.749	0.9281	0.2076

(b) Effect of Prior on UHD low-light image enhancement.

Prior	PSNR \uparrow	SSIM \uparrow	LPIPS \downarrow
w/o Priors	26.102	0.9196	0.2405
w/o Gradient	26.002	0.9253	0.2137
w/o Normal	26.975	0.9272	0.2096
Full (Ours)	26.749	0.9281	0.2076

(c) Effect of PFI on UHD image desnowing.

Module	PSNR \uparrow	SSIM \uparrow	LPIPS \downarrow
w/o PFI	37.204	0.9886	0.0248
w/o DPFI	37.544	0.9886	0.0247
w/o SPFI	38.189	0.9891	0.0237
Full (Ours)	39.350	0.9894	0.0230

(d) Effect of Prior on UHD image desnowing.

Prior	PSNR \uparrow	SSIM \uparrow	LPIPS \downarrow
w/o Priors	28.540	0.9764	0.0583
w/o Gradient	38.618	0.9892	0.0241
w/o Normal	38.816	0.9891	0.0234
Full (Ours)	39.350	0.9894	0.0230

(e) Effect of PFI on UHD image deraining.

Module	PSNR \uparrow	SSIM \uparrow	LPIPS \downarrow
w/o PFI	37.824	0.9752	0.0554
w/o DPFI	37.877	0.9758	0.0548
w/o SPFI	37.825	0.9756	0.0535
Full (Ours)	38.072	0.9765	0.0522

(f) Effect of Prior on UHD image deraining.

Prior	PSNR \uparrow	SSIM \uparrow	LPIPS \downarrow
w/o Priors	33.096	0.9530	0.1329
w/o Gradient	37.966	0.9765	0.0535
w/o Normal	38.005	0.9757	0.0546
Full (Ours)	38.072	0.9765	0.0522

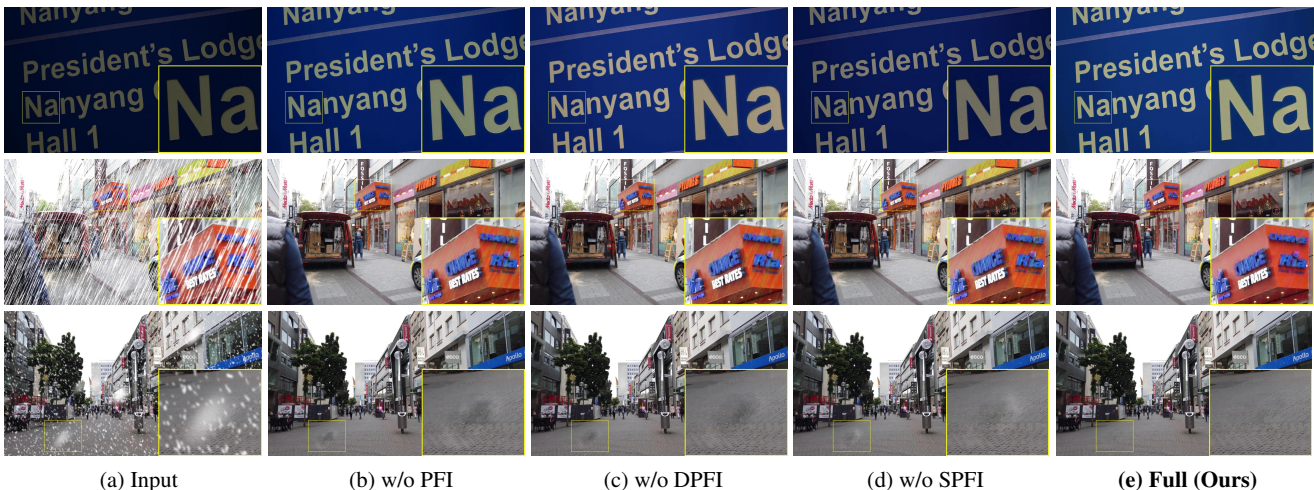


Fig. 13 Visual comparison on each component in PFI on UHD low-light image enhancement, deraining, and desnowing (from top to bottom).

the effect on the number of prior feature interaction (L), the effect on the number of channels (C), the effect on the shuffle down factor (S), the effect on the shuffle down factor (D) in dual prior feature interaction, and the effect on loss functions. Finally, we provide the analysis for generalization on different resolutions. Experiments are performed on the UHD-LL (Li et al., 2023), and models are trained on the patch of size 512×512 for 60K iterations.

Effect on Number of Prior Feature Interaction (L).

In the prior feature interaction branch of UHDDIP, we analyze the impact on the number of prior feature interaction (PFI) modules for model performance. Table 8 demonstrates that performance incrementally improves as the number of PFI increases, alongside the number of parameters. However, using 4 PFI modules degrades the network's performance, whereas 3 PFI modules perform the best. We further present visual results, as illustrated in Fig. 15. We note that a single PFI module often has difficulty removing the enhanced noise. Using 2 PFI modules can effectively

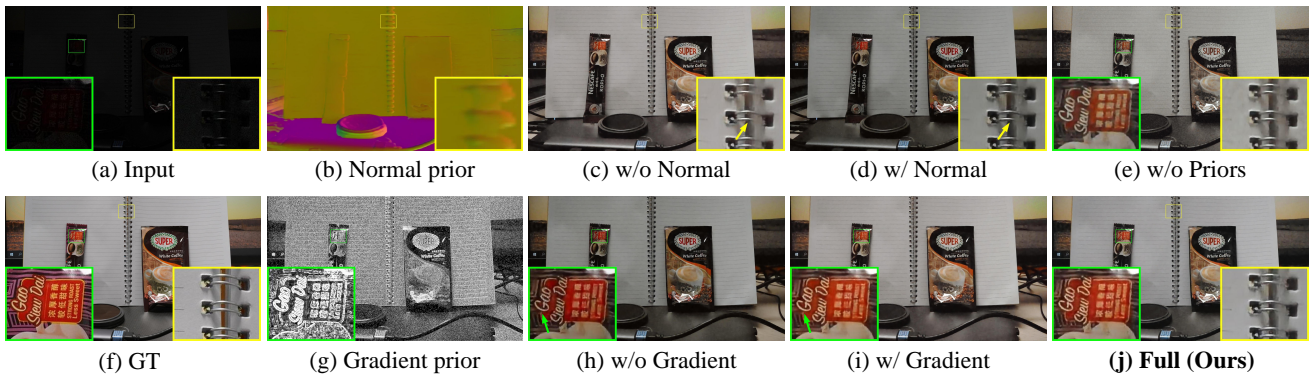


Fig. 14 Visual comparison of adopting different priors in the low-resolution branch on UHD low-light image enhancement.

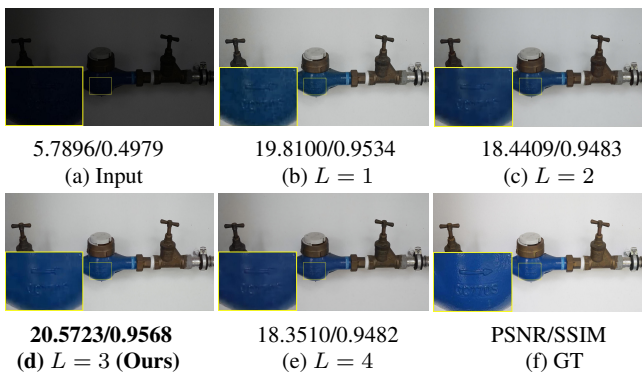


Fig. 15 Visualization results on different numbers of PFI modules (L). Our model with 3 PFI modules obtains results more desirable than others.

Table 8 Effect on Number of Prior Feature Interaction (L). The model with 3 PFI modules achieves the best performance.

Number L of PFI	PSNR \uparrow	SSIM \uparrow	LPIPS \downarrow
$L = 1$	25.902	0.9227	0.2336
$L = 2$	26.352	0.9254	0.2162
$L = 3$ (Ours)	26.749	0.9281	0.2076
$L = 4$	26.479	0.9269	0.2077

remove noise, but it challenges color restoration. The desirable results are produced using 3 PFI modules. However, 4 PFI modules will bring about a color difference, which may be because too many PFI modules make excessive interactions between prior features deteriorate the final result.

Effect on Number of Channels (C). We measure the impact on the number of channels in all modules, as seen in Table 9. It can be noticed that SSIM and LPIPS metrics improve as the number of channels increases. Our method with 16 channels achieves optimal PSNR performance. However, increasing the number of channels to 32 results in signifi-

Table 9 Effect on Number of Channels (C). The model with 16 channels achieves the best performance in terms of PSNR.

Channels C	PSNR \uparrow	SSIM \uparrow	LPIPS \downarrow
$C = 8$	26.602	0.9244	0.2498
$C = 16$ (Ours)	26.749	0.9281	0.2076
$C = 32$	26.192	0.9283	0.1997

Table 10 Effect on Shuffle-Down Factor (S). The model with the shuffle-down factor of 8 is optimal.

Factor S	PSNR \uparrow	SSIM \uparrow	LPIPS \downarrow
$S = 4$	26.415	0.9259	0.2078
$S = 8$ (Ours)	26.749	0.9281	0.2076
$S = 16$	26.492	0.9244	0.2169

Table 11 Effect on Shuffle-Down Factor (D) in DPFI. The model with the shuffle-down factor of 4 obtains the best performance in terms of PSNR and SSIM.

Factor D in DPFI	PSNR \uparrow	SSIM \uparrow	LPIPS \downarrow
$D = 2$	26.330	0.9261	0.2061
$D = 4$ (Ours)	26.749	0.9281	0.2076
$D = 8$	26.389	0.9250	0.2160

Table 12 Effect on Loss Functions. The model with total loss obtains the best performance.

Loss Function	PSNR \uparrow	SSIM \uparrow	LPIPS \downarrow
(a) w/o low-resolution loss	26.072	0.9248	0.2128
(b) Total loss (Ours)	26.749	0.9281	0.2076

cant degradation of PSNR performance and increases the number of parameters by approximately 3.8 times. Thus, we finally set C as 16 to make a trade-off between performance and computational cost. In addition, we also provide a visual example in Fig. 16. One can observe that when the channel is set as 8, the recovered result still exhibits some

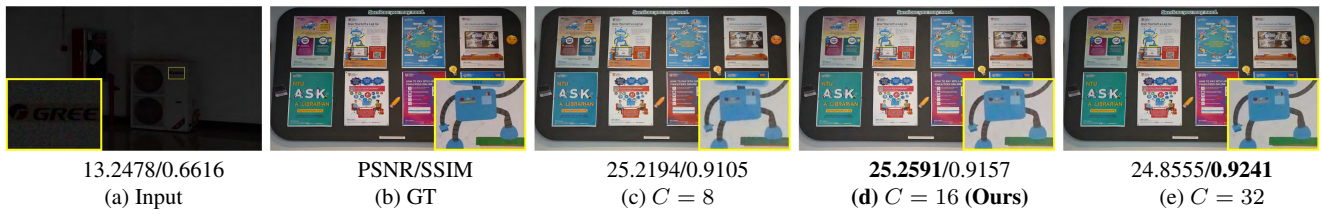


Fig. 16 Visualization results on different numbers of channels C . Our model with 16 channels strikes a balance, producing results with enhanced texture details and more natural colors.

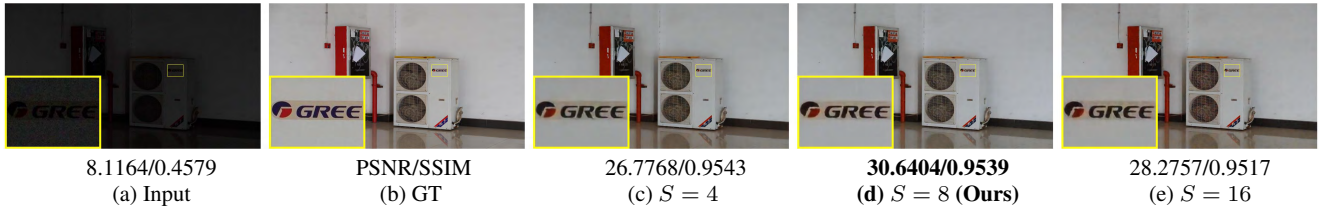


Fig. 17 Visualization results on Shuffle-Down Factor S . Our model with the shuffle-down factor of 8 is able to generate results with clearer structures and colors closer to GT.

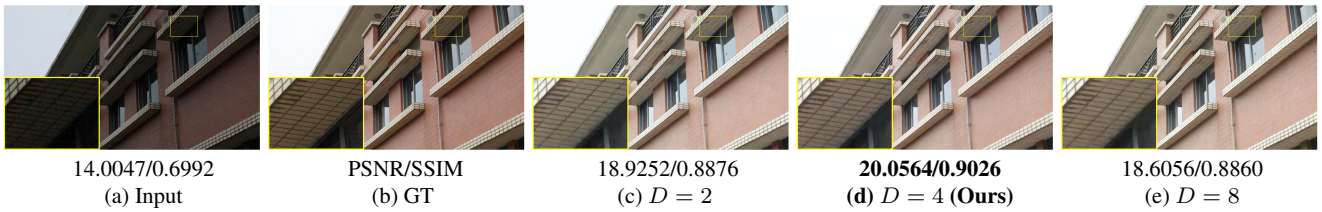


Fig. 18 Visual effect on the Shuffle-Down Factor D in DPFI. Our model with the shuffle-down factor of 4 in DPFI is able to generate results with clearer structure and more details.

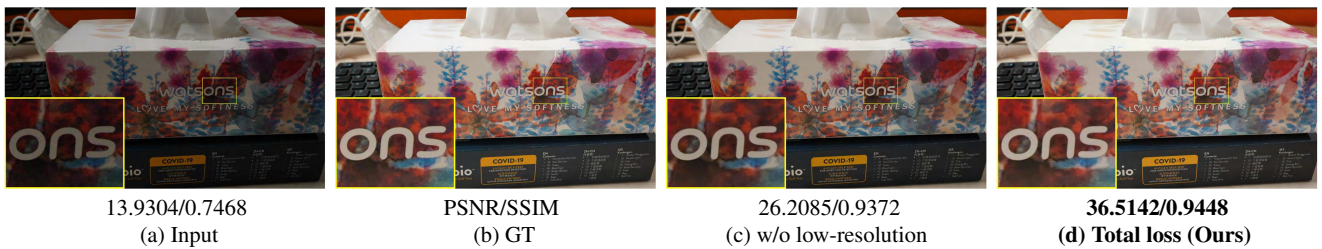


Fig. 19 Visualization results on different loss functions. Our model with total loss is able to generate a clearer structure and colors closer to GT.

noise and poor colors. Conversely, when the channel is set as 32, the colors are better recovered, but they appear overly smooth, resulting in a loss of detailed textures. In contrast, our model with 16 channels strikes a balance, producing results with enhanced texture details and more natural colors.

Effect on Shuffle-Down Factor (S). Table 10 provides an ablation experiment on shuffle-down factor including $S = 4$, $S = 8$, and $S = 16$. As can be seen, our model

with the shuffle-down factor of 8 is optimal. This suggests that using a resolution that is either too large or too small is detrimental to image recovery. Fig. 17 shows a visual result. It is evident that the model with a shuffle-down factor of 8 delivers superior visual quality compared to the other factor.

Effect on Shuffle-Down Factor (D) in Dual Prior Feature Interaction. To reduce the computational burden, we initially perform a shuffle-down operation on two

Table 13 UHD low-light image enhancement by using the LOL training dataset (Wei et al., 2018) and then testing on UHD-LL testing dataset. The best and second best are marked in **bold** and underlined, respectively.

Type	Methods	Venue	PSNR \uparrow	SSIM \uparrow	LPIPS \downarrow
General	Restormer (Zamir et al., 2022)	CVPR'22	17.728	0.7703	0.4566
	Uformer (Wang et al., 2022b)	CVPR'22	18.168	0.7201	0.5593
UHD	LLFormer (Wang et al., 2023b)	AAAI'23	21.440	0.7763	0.4528
	UHDFour (Li et al., 2023)	ICLR'23	14.771	0.3760	0.7608
	UHDformer (Wang et al., 2024b)	AAAI'24	22.615	<u>0.7754</u>	<u>0.4241</u>
	UHDDIP (Ours)	-	<u>22.287</u>	0.7898	0.4239

**Fig. 20** Visual results of UHD low-light image enhancement trained on the LOL dataset. Our UHDDIP can generate clearer results.

prior features in DPFI. Table 11 examines the impact of various shuffle-down factors on the model's performance. The results indicate that the network achieves optimal PSNR and SSIM with a shuffle-down factor of 4. A visual example is provided in Fig. 18. One can observe that, with a shuffle-down factor of 4, the restored result on structures and details can be more desirable than others, which illustrates the effectiveness of this configuration.

Effect on Loss Functions. In our method, we supervise not only the high-resolution space, but also the

low-resolution space. Hence, we are necessary to analyze the effect on loss functions. Table 12 shows that constraining both the high-resolution branch and the low-resolution branch together gains 0.677dB PSNR gain compared to constraining only the high-resolution branch while having a similar number of parameters. The finding suggests that significant enhancements can be achieved by applying an additional loss function to the low-resolution branch. This improvement likely stems from the greater utility of prior feature constraints in facilitating image recovery. From Fig. 19, we can see that the model trained with the total loss

Table 14 Efficiency comparison. We report the number of parameters, FLOPs, and running time. The testing is conducted on a single RTX2080Ti GPU with a batch size of 1 at a resolution of 1024×1024 .

Methods	Type	Parameters (M) ↓	FLOPs (G) ↓	Running Time (s) ↓
Restormer (Zamir et al., 2022)	General	26.10	2255.85	1.86
Uformer (Wang et al., 2022b)		20.60	657.45	0.60
SFNet (Cui et al., 2023)		13.23	1991.03	0.61
DehazeFormer (Song et al., 2023)		2.51	375.40	0.45
Stripformer (Tsai et al., 2022)		19.71	2728.08	0.15
FFTformer (Kong et al., 2023)		16.56	2104.60	1.27
LLFormer (Wang et al., 2023b)	UHD	13.13	221.64	1.69
UHD (Zheng et al., 2021)		34.55	113.45	0.04
UHDFour (Li et al., 2023)		17.54	75.63	0.02
UHDformer (Wang et al., 2024b)		0.34	48.37	0.16
UHDDIP (Ours)		0.81	34.73	0.13

function performs better, generating results with a clearer structure and colors closer to GT.

Analysis for the generalization on different resolutions. To deeper understanding of how models trained on low-resolution datasets generalize to UHD images, we conduct experiments on low-light image enhancement. We retrain our model alongside several baseline methods using the low-resolution dataset LOL (Wei et al., 2018) and test these models on UHD-LL. The results are reported in Table 13. As we can see, our UHDDIP performs outstandingly in SSIM and LPIPS scores, which is consistent with the results obtained by training on UHD-LL datasets and further illustrates that our model has generalizability on datasets of different resolutions. Fig. 20 provides visual results of UHD low-light image enhancement trained on the LOL dataset, where our UHDDIP is able to generate clearer results and visually closer to the ground truth.

5.5 Computational Complexity

Table 14 showcases the efficiency of various methods regarding the number of parameters, FLOPs, and running time. These results are obtained on a single RTX2080Ti GPU, using a batch size of 1 at a resolution of 1024×1024 . We observed that the proposed UHDDIP is effective, with significant improvements in parameters and FLOPs compared to the general IR methods including Uformer (Wang et al., 2022b), Restormer (Zamir et al., 2022), SFNet (Cui et al., 2023), DehazeFormer (Song et al., 2023), Stripformer (Tsai et al., 2022), and FFTformer (Kong et al., 2023), and methods for a specific design for UHD restoration, e.g., LLFormer (Wang et al., 2023b), UHD-Four (Li et al., 2023), UHD (Zheng et al., 2021), and UHDformer (Wang et al., 2024b). Especially, our UHDDIP reduces by 28.2% and 18.8% in FLOPs and running time compared to UHDformer (Wang et al., 2024b), whereas it causes only a slight increase in parameters. In conclusion, UHD-

DIP only increases a small number of parameters but significantly reduces computational complexity while achieving good performance.

6 Conclusion

In this paper, we have conducted new UHD benchmarks, including UHD-Snow and UHD-Rain to remedy the research on UHD image desnowing and deraining. We have further proposed a dual interaction prior-driven UHD restoration method (UHDDIP) to address the problem of missing image details and structures in UHD restoration. It is built around a prior feature interaction module containing SPFI and DPFI, that incorporates gradient and normal priors into model design to achieve high-quality restoration with finer structures and details. Experimental results have shown that UHDDIP can achieve state-of-the-art performance on 5 tasks, including UHD low-light image enhancement, dehazing, deblurring, desonwing, and deraining.

Data Availability Statement. UHD datasets and pre-trained models used in this paper are available online. We provide corresponding source links for reproduction purposes in the UHDDIP repository <https://github.com/wlydlut/UHDDIP>.

References

- Buades A, Coll B, Morel J (2005) A non-local algorithm for image denoising. In: CVPR, pp 60–65
- Chen L, Lu X, Zhang J, Chu X, Chen C (2021a) Hinet: Half instance normalization network for image restoration. In: CVPR Workshops, pp 182–192
- Chen L, Chu X, Zhang X, Sun J (2022) Simple baselines for image restoration. In: ECCV, vol 13667, pp 17–33
- Chen W, Fang H, Ding J, Tsai C, Kuo S (2020a) JSTASR: joint size and transparency-aware snow removal algorithm based on modified partial convolution and veiling effect removal. In: ECCV, vol 12366, pp 754–770

- Chen W, Fang H, Ding J, Tsai C, Kuo S (2020b) JSTASR: joint size and transparency-aware snow removal algorithm based on modified partial convolution and veiling effect removal. In: ECCV, vol 12366, pp 754–770
- Chen W, Fang H, Hsieh C, Tsai C, Chen I, Ding J, Kuo S (2021b) ALL snow removed: Single image desnowing algorithm using hierarchical dual-tree complex wavelet representation and contradict channel loss. In: ICCV, pp 4176–4185
- Chen WT, Fang HY, Hsieh CL, Tsai CC, Chen I, Ding JJ, Kuo SY, et al. (2021c) All snow removed: Single image desnowing algorithm using hierarchical dual-tree complex wavelet representation and contradict channel loss. In: ICCV, pp 4196–4205
- Chen X, Pan J, Lu J, Fan Z, Li H (2023) Hybrid cnn-transformer feature fusion for single image deraining. In: AAAI, pp 378–386
- Cho S, Ji S, Hong J, Jung S, Ko S (2021) Rethinking coarse-to-fine approach in single image deblurring. In: ICCV, pp 4621–4630
- Cui Y, Tao Y, Bing Z, Ren W, Gao X, Cao X, Huang K, Knoll A (2023) Selective frequency network for image restoration. In: ICLR
- Deng S, Ren W, Yan Y, Wang T, Song F, Cao X (2021) Multi-scale separable network for ultra-high-definition video deblurring. In: ICCV, pp 14010–14019
- Dong C, Loy CC, He K, Tang X (2016) Image super-resolution using deep convolutional networks. *IEEE TPAMI* 38(2):295–307
- Dosovitskiy A, Beyer L, Kolesnikov A, Weissenborn D, Zhai X, Unterthiner T, Dehghani M, Minderer M, Heigold G, Gelly S, et al. (2021) An image is worth 16x16 words: Transformers for image recognition at scale. In: ICLR
- Eftekhari A, Sax A, Malik J, Zamir A (2021) Omnidata: A scalable pipeline for making multi-task mid-level vision datasets from 3d scans. In: ICCV, pp 10766–10776
- He K, Zhang X, Ren S, Sun J (2016) Deep residual learning for image recognition. In: CVPR, pp 770–778
- Huang H, Yu A, Chai Z, He R, Tan T (2021) Selective wavelet attention learning for single image deraining. *IJCV* 129(4):1282–1300
- Huynh-Thu Q, Ghanbari M (2008) Scope of validity of psnr in image/video quality assessment. *Electronics Letters* 44(13):800–801
- Kong L, Dong J, Ge J, Li M, Pan J (2023) Efficient frequency domain-based transformers for high-quality image deblurring. In: CVPR, pp 5886–5895
- Krizhevsky A, Sutskever I, Hinton GE (2012) Imagenet classification with deep convolutional neural networks. In: NeurIPS, pp 1106–1114
- Lee HS, Cho SI (2023) Locally adaptive channel attention-based spatial-spectral neural network for image deblurring. *IEEE TCSVT* 33(10):5375–5390
- Li C, Guo C, Zhou M, Liang Z, Zhou S, Feng R, Loy CC (2023) Embedding fourier for ultra-high-definition low-light image enhancement. In: ICLR
- Li S, Ren W, Wang F, Araujo IB, Tokuda EK, Junior RH, Jr RMC, Wang Z, Cao X (2021) A comprehensive benchmark analysis of single image deraining: Current challenges and future perspectives. *IJCV* 129(4):1301–1322
- Liang J, Cao J, Sun G, Zhang K, Van Gool L, Timofte R (2021) SwinIR: Image restoration using swin transformer. In: ICCV Workshops
- Loshchilov I, Hutter F (2017) SGDR: Stochastic gradient descent with warm restarts. In: ICLR
- Lu L, Li W, Tao X, Lu J, Jia J (2021) MASA-SR: matching acceleration and spatial adaptation for reference-based image super-resolution. In: CVPR, pp 6368–6377
- Luo Y, Xu Y, Ji H (2015) Removing rain from a single image via discriminative sparse coding. In: ICCV, pp 3397–3405
- Mei Y, Fan Y, Zhang Y, Yu J, Zhou Y, Liu D, Fu Y, Huang TS, Shi H (2023) Pyramid attention network for image restoration. *IJCV* 131(12):3207–3225
- Song Y, He Z, Qian H, Du X (2023) Vision transformers for single image dehazing. *IEEE TIP* 32:1927–1941
- Tsai F, Peng Y, Lin Y, Tsai C, Lin C (2022) Stripformer: Strip transformer for fast image deblurring. In: ECCV, vol 13679, pp 146–162
- Tu Z, Talebi H, Zhang H, Yang F, Milanfar P, Bovik AC, Li Y (2022) MAXIM: multi-axis MLP for image processing. In: CVPR, pp 5759–5770
- Wang C, Wu Y, Su Z, Chen J (2020a) Joint self-attention and scale-aggregation for self-calibrated deraining network. In: ACM MM, pp 2517–2525
- Wang C, Xing X, Wu Y, Su Z, Chen J (2020b) DCSFN: deep cross-scale fusion network for single image rain removal. In: ACM MM, pp 1643–1651
- Wang C, Xing X, Yao G, Su Z (2021) Single image deraining via deep shared pyramid network. *TVC* 37:1851–1865
- Wang C, Pan J, Wu XM (2022a) Online-updated high-order collaborative networks for single image deraining. In: AAAI, vol 36, pp 2406–2413
- Wang C, Pan J, Wang W, Dong J, Wang M, Ju Y, Chen J (2023a) Promptrestorer: A prompting image restoration method with degradation perception. In: NeurIPS
- Wang C, Pan J, Lin W, Dong J, Wang W, Wu XM (2024a) Selfpromer: Self-prompt dehazing transformers with depth-consistency. In: AAAI, vol 38, pp 5327–5335
- Wang C, Pan J, Wang W, Fu G, Liang S, Wang M, Wu XM, Liu J (2024b) Correlation matching transformation transformers for uhd image restoration. In: AAAI, vol 38, pp 5336–5344
- Wang C, Wang W, Yu C, Mu J (2024c) Explore internal and external similarity for single image deraining with graph neural networks. In: IJCAI, pp 1371–1379

- Wang T, Zhang K, Shen T, Luo W, Stenger B, Lu T (2023b) Ultra-high-definition low-light image enhancement: A benchmark and transformer-based method. In: AAAI
- Wang Z, Bovik AC, Sheikh HR, Simoncelli EP (2004) Image quality assessment: from error visibility to structural similarity. *IEEE TIP* 13(4):600–612
- Wang Z, Cun X, Bao J, Liu J (2022b) Uformer: A general u-shaped transformer for image restoration. In: CVPR
- Wang Z, Yan Z, Yang MH, Pan J, Yang J, Tai Y, Gao G (2024) Scene Prior Filtering for Depth Map Super-Resolution. *arXiv e-prints arXiv:2402.13876*, DOI 10.48550/arXiv.2402.13876, [2402.13876](https://arxiv.org/abs/2402.13876)
- Wei C, Wang W, Yang W, Liu J (2018) Deep retinex decomposition for low-light enhancement. In: BMVC, p 155
- Xu L, Zheng S, Jia J (2013) Unnatural L0 sparse representation for natural image deblurring. In: CVPR, pp 1107–1114
- Yang W, Tan RT, Feng J, Liu J, Guo Z, Yan S (2017) Deep joint rain detection and removal from a single image. In: CVPR, pp 1685–1694
- Yang W, Tan RT, Feng J, Guo Z, Yan S, Liu J (2020) Joint rain detection and removal from a single image with contextualized deep networks. *IEEE TPAMI* 42(6):1377–1393
- Yang Y, Wang C, Guo X, Tao D (2024) Robust unpaired image dehazing via density and depth decomposition. *IJCV* 132(5):1557–1577
- Yao G, Wang C, Wu Y, Wang Y (2021) Pyramid fully residual network for single image de-raining. *Neurocomputing* 456:168–178
- Zamir SW, Arora A, Khan SH, Hayat M, Khan FS, Yang M, Shao L (2021) Multi-stage progressive image restoration. In: CVPR, pp 14821–14831
- Zamir SW, Arora A, Khan S, Hayat M, Khan FS, Yang M (2022) Restormer: Efficient transformer for high-resolution image restoration. In: CVPR, pp 5718–5729
- Zhang H, Li Y, Chen H, Gong C, Bai Z, Shen C (2022a) Memory-efficient hierarchical neural architecture search for image restoration. *IJCV* 130(1):157–178
- Zhang K, Zuo W, Chen Y, Meng D, Zhang L (2017) Beyond a gaussian denoiser: Residual learning of deep CNN for image denoising. *IEEE TIP* 26(7):3142–3155
- Zhang K, Li D, Luo W, Ren W, Stenger B, Liu W, Li H, Yang M (2021a) Benchmarking ultra-high-definition image super-resolution. In: ICCV, pp 14749–14758
- Zhang K, Li Y, Zuo W, Zhang L, Gool LV, Timofte R (2022b) Plug-and-play image restoration with deep denoiser prior. *IEEE TPAMI* 44(10):6360–6376
- Zhang R, Isola P, Efros AA, Shechtman E, Wang O (2018) The unreasonable effectiveness of deep features as a perceptual metric. In: CVPR, pp 586–595
- Zhang Y, Tian Y, Kong Y, Zhong B, Fu Y (2021b) Residual dense network for image restoration. *IEEE TPAMI* 43(7):2480–2495
- Zhao L, Lu S, Chen T, Yang Z, Shamir A (2021) Deep symmetric network for underexposed image enhancement with recurrent attentional learning. In: ICCV, pp 12055–12064
- Zheng Z, Ren W, Cao X, Hu X, Wang T, Song F, Jia X (2021) Ultra-high-definition image dehazing via multi-guided bilateral learning. In: CVPR, pp 16185–16194